Materials and Design 202 (2021) 109533

Contents lists available at ScienceDirect

Materials and Design

journal homepage: www.elsevier.com/locate/matdes

Laser welding of H-phase strengthened Ni-rich NiTi-20Zr high temperature shape memory alloy

J.P. Oliveira [a,*], Jiajia Shen [a], J.D. Escobar [b], C.A.F. Salvador [c], N. Schell [d], N. Zhou [e], O. Benafan [f]

[a] UNIDEMI, Department of Mechanical and Industrial Engineering, NOVA School of Science and Technology, Universidade NOVA de Lisboa, 2829-516, Caparica, Portugal
[b] Metallurgical and Materials Engineering Department, University of São Paulo, Av. Prof. Mello Moraes 2463, 05508-030, São Paulo, SP, Brazil
[c] University of Sao Paulo (USP), Institute of Physics, São Paulo, SP 05508-090, Brazil
[d] Institute of Materials Research, Helmholtz-Zentrum Geesthacht, Max-Planck-Str. 1, D-21502 Geesthacht, Germany
[e] Centre for Advanced Materials Joining, University of Waterloo, Canada
[f] NASA Glenn Research Center, Materials and Structures Division, Cleveland, OH 44135, USA

HIGHLIGHTS

- Laser welding of an H-phase strengthened NiTi-20Zr high-temperature shape memory alloy was successfully performed.
- The aged NiTi-20Zr experienced partial H-phase dissolution in the heat-affected zone.
- The welded joints sustain stresses typically used in actuator applications (up to 500 MPa).

GRAPHICAL ABSTRACT

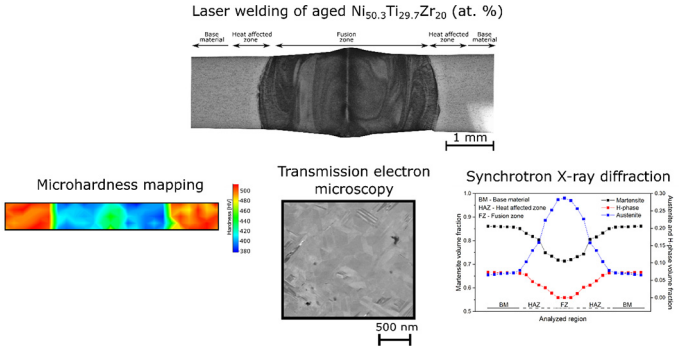

ARTICLE INFO

Article history:
Received 5 January 2021
Received in revised form 22 January 2021
Accepted 26 January 2021
Available online 29 January 2021

Keywords:
NiTiZr
High temperature shape memory alloys
Laser welding
Synchrotron X-ray diffraction
Rietveld refinement
H-phase

ABSTRACT

Laser welding of a Ni-rich NiTi-20Zr (at.%) high temperature shape memory alloy was performed. The starting base material was aged for 3 h at 550 °C followed by air cooling prior to welding to induce H-phase precipitation. Advanced microstructure characterization encompassing scanning and transmission electron microscopy, coupled with synchrotron X-ray diffraction, were used. Defect-free welds were obtained with a conduction welding mode. The weld thermal cycle altered the microstructure across the heat affected and fusion zones of the joints. The heat affected zone exhibited partial H-phase dissolution, causing a decrease in hardness. In the fusion zone, the H-phase fully dissolved, and the non-equilibrium rapid solidification conditions prevented the H-phase from re-precipitating during cooling, leading to a microstructure resembling that of an as-cast alloy with the same material composition. Mechanical testing revealed that the laser welded samples sustained stresses in the order of 500 MPa and exhibited stress-strain responses comparable to those of the unwelded base material. Thus, this initial study shows new possibilities for using advanced laser joining methods in these alloys.

* Corresponding author.
E-mail address: jp.oliveira@fct.unl.pt (J.P. Oliveira).

https://doi.org/10.1016/j.matdes.2021.109533

1. Introduction

Shape memory alloys (SMAs) possess remarkable functional properties, enabled via the shape memory effect and their superelastic behaviors. From a large alloy formulation, the NiTi-based alloy family is the most studied of these SMAs. Dating back to its discovery by Buehler et al. in the 1960s, significant research efforts have transpired to understand the microstructure and property relationships in NiTi [1], leading to multiple applications in various fields [2–5]. Nonetheless, widely used binary NiTi and prominent ternary additions such as NiTiFe or NiTiNb exhibit transformation temperatures below 100 °C, limiting their applicability at higher temperatures (e.g., in aeronautics and automotive fields). To overcome this limitation, alloying with elements such as Zr, Hf, Pt, and Au has been used to increase the transformation temperatures, with reasonable success. Of particular interest, the addition of Hf and Zr have resulted in favorable properties while maintaining a relatively lower cost compared to the Pt, Pd, and Au counterparts. As such, the majority of recent work on NiTi-based high temperature shape memory alloys has been devoted to NiTiHf and NiTiZr alloys, with special emphasis on the former system [6–8].

Despite this greater focus on the NiTiHf system, NiTiZr alloys are emerging as potential compositions, sharing many similar attributes with NiTiHf alloys. NiTiZr alloys demonstrate comparable thermomechanical properties while being roughly 23% lighter and 28% less expensive than NiTiHf alloys for the same composition (i.e., 20Hf compared to 20Zr) [9–11]. It was also recently shown that good transformational properties (temperature, strain, and dimensional stability) are obtained when replacing Zr for Hf in a $Ni_{50.3}Ti_{29.7}(Hf,Zr)_{20}$ (at.%) alloy [12]. Therefore, to further advance the adoption of this alloy, understanding its thermomechanical processability by various manufacturing methods is imperative.

One of the potential processing methods that can be applied for critical components is joining and welding. To date, there are no weldability studies performed on NiTiZr high temperature SMAs. In our previous work, it was shown that a NiTiHf counterpart exhibited excellent weldability when using a laser as the heat source for similar joining [13]. No detrimental effects caused by the typical changed microstructure development in both the heat affected and fusion zones were observed. Similar welding methods can be applied to NiTiZr, but the high temperatures experienced by the fusion zone and its surroundings can promote oxidation due to the extremely high affinity of Zr to oxygen, even under vacuum conditions [14]. Although previous work on the NiTiHf system has shown that these high temperature alloys can be laser welded, investigating if the exchange of Hf by Zr influences the material weldability is fundamental.

In this work, laser welding of an aged NiTiZr high temperature SMA was performed for the first time. The microstructure evolution is studied by means of optical, scanning and transmission electron microscopy coupled with synchrotron X-ray diffraction. Assessment of the joints mechanical properties was evaluated via tensile testing at both room temperature and high temperature (200 °C) conditions. in the mart

2. Experimental procedure

A Ni-rich alloy with a target composition of $Ni_{50.3}Ti_{29.7}Zr_{20}$ (at.%) was produced using vacuum induction skull melting with a batch size of 27 kg (designated as FS#Z1). Molten metal was cast into 30.5 mm rods, subjected to a homogenization heat treatment of 1050 °C for 72 h, and furnace cooled. The rods were then hot-extruded at 900 °C at an area reduction ratio of 7:1. The material was then aged at 550 °C for 3 h, followed by air cooling to allow for H-phase precipitation. Wire electrical discharge machining (EDM) followed by centerless grinding lead to a final rod diameter of 1.59 mm.

A Nd:YAG ($\lambda = 1064$ nm) Unitek LW50A laser from Miyachi was used for the welding experiments. The laser had a top-hat profile. Single-pulse welded joints were obtained using a pulse energy of 37.5 J. The pulse profile included an upslope ramp of 4 ms duration, a plateau at 2.35 kW peak power of 12 ms, and a downslope ramp of 4 ms. The laser beam was focused on the base material surface to a diameter of 600 μm. Argon was used as shielding gas to reduce oxidation. The experimental setup used in this work is similar to that used in [15,16]. Prior to welding, samples to be joined were cleaned. Preliminary tests on sacrificial samples were performed to achieve full penetration and defect-free joints. Due to the lack of available material, this research focused on obtaining a set of parameters capable of ensure joints with not discernible defects. This paper describes the microstructure evolution and mechanical behavior of those joints.

The as-welded material was prepared for microstructure characterization using standard metallographic preparation techniques. To reveal the microstructure, an etching solution composed of H_2O:HNO_3:HF (10:5:1 in volume) was used for 5 s. Scanning electron microscopy (SEM) using a Quanta 200 SEM equipped with an energy-dispersive spectroscopy (EDS) detector was used to analyse the fusion zone microstructure. Scanning transmission electron microscopy (STEM) was used for nanoscale analysis of the fusion zone. A site-specific thin foil of the fusion zone was prepared by focused ion beam (FIB) using a Helios NanoLab 600 DualBeam. STEM imaging and compositional measurements were performed using a Tecnai G2–30 TEM operating at 200 keV.

Further mesoscale microstructure characterization was performed using high-energy synchrotron X-ray diffraction. These measurements were performed at the P07 High-Energy Materials Science Beamline at Petra III/DESY. The high photon energy (87.1 keV) allowed for transmission mode measurements, which enabled the determination of bulk microstructure information. A square shaped beam of 200×200 μm^2 was used to probe the processed material. These measurements started in the non-affected base material, crossed the heat affected and fusion zones, and ended at the other end of the base material. The distance between consecutive points was 200 μm. The wavelength used in this experiment was 0.14235 Å and the sample-to-detector distance was determined to be 1527 mm using LaB_6 calibrant powder. The LaB_6 powder was also used to estimate the instrumental peak broadening associated with the beamline. The 2D raw images, acquired using a PerkinElmer fast detector, were treated with a combination of Fit2D [17,18] and MAUD (Materials Analysis Using Diffraction) [19,20]. Rietveld refinement was performed to determine the lattice parameters of austenite, martensite, and (when present) H-phase across the material, as well as their volume fractions using MAUD [19–21]. A schematic of the experimental setup and definition of the azimuthal angle, ϕ, are detailed in Fig. 1.

Assessment of the mechanical properties was performed using an MTS Insight load frame. Specimens ~200 mm long were mounted on the grips and pulled in uniaxial tension between 500 and 800 MPa at a stress rate of 40 MPa/min. Strains were measured using a GOM ARAMIS digital image correlation (DIC) optical metrology system. For elevated temperature testing, an MTS Advantage environmental chamber equipped with a Eurotherm temperature controller was used. Samples were heated to 200 °C, pulled in uniaxial tension to 500 MPa, and then unloaded to 0 MPa. For reference, the base material (unwelded sample) was subjected to the same mechanical loading. Due to the limited number of specimens for mechanical testing, it was decided to only subject the joints to a load/unload cycle in the low and high temperature regimes. Such allows to have a preliminary understanding of the mechanical strength of the joints and the potential of laser welding as a joining technique for these advanced materials.

Differential scanning calorimetry (DSC) tests were conducted using a TA Instruments Q1000 device. Base material samples were thermally cycled 10 times between −150 and 380 °C using a heating/cooling rate of 10 °C/min. Only the last cycle data are shown in Fig. 2. The transformation temperatures of the base material as determined by the derivative method are detailed in Table 1, where it can be observed that a shift of the transformation

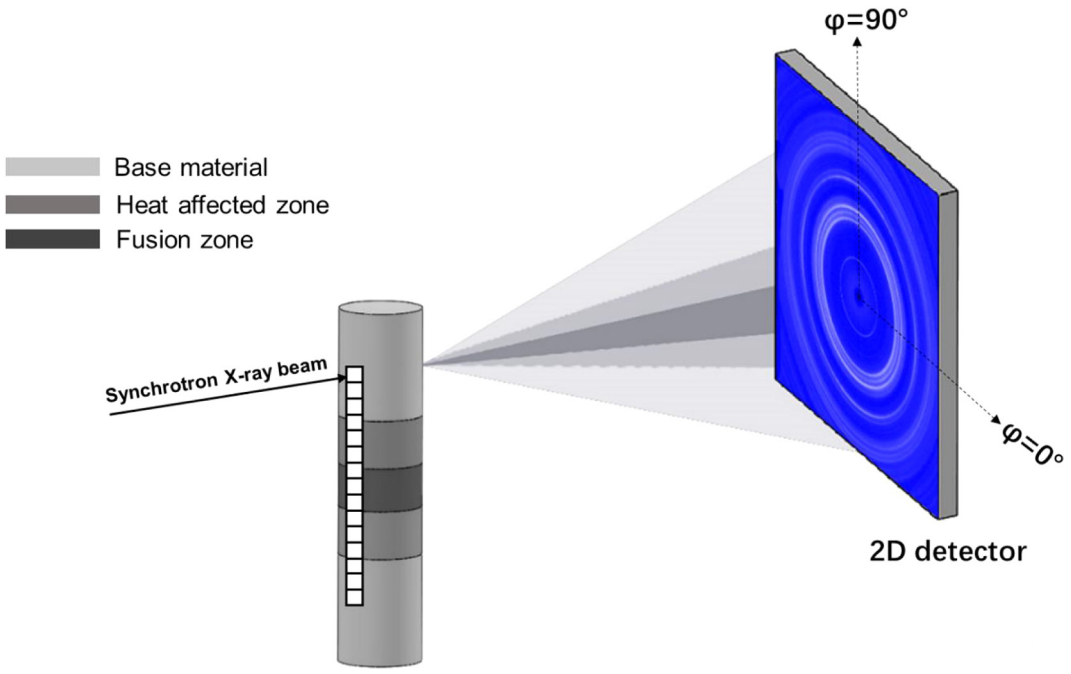

Fig. 1. Synchrotron X-ray diffraction setup (not to scale), highlighting the laboratorial reference for the azimuthal angle, ϕ.

temperature to higher temperatures occurred upon aging at 550 °C for 3 h. This can be explained based on the matrix Ni depletion that occurs upon H-phase precipitation. As a result of the decrease of the Ni content in the matrix the transformation temperatures increase. Due to the reduced dimensions of both the heat-affected and fusion zones, no DSC analysis of these regions were performed since mixed microstructural information would be obtained.

Hardness mapping along the welded joints (i.e., base material, heat affected and fusion zones) was performed to evaluate the welding effects. These hardness measurements were performed using a 300 g load, and the space between consecutive indentations was 200 μm along the vertical and horizontal directions.

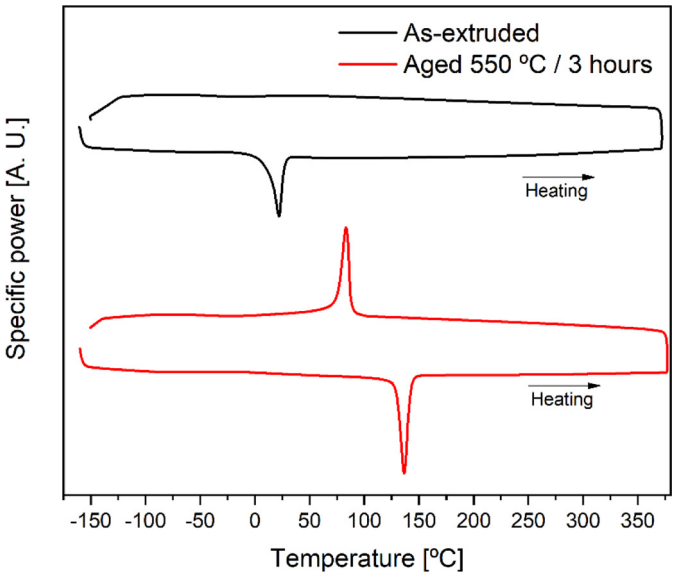

Fig. 2. Differential scanning calorimetry curves of the as-extruded and aged NiTi-20Zr base material.

3. Results and discussion

3.1. Microstructure evolution

Optical micrographs of a representative weld cross-section are depicted in Fig. 3a. A full-penetration, defect-free joint was obtained under the selected laser welding parameters. Within the fusion zone, the effects of the Marangoni currents on the material flow can be observed, although a fully dendritic region is found in this region, as typical of fusion-based welding processes. The material flow due to surface tension in the melt pool can be influenced by the elemental composition and the local temperatures, which are known to vary across this region [22].

Typically, two welding modes can occur during high power beam welding dependent on the width-to-depth ratio of the fusion zone. If the aspect ratio (width/depth ratio) is significantly larger than unity, conduction welding occurs; otherwise, keyhole mode is favored. In this work, conduction mode welding is observed. It should be noted that it is not only the geometry or thermophysical properties of the material that promote conduction or keyhole welding modes, but also the process parameters, including laser power and energy or defocusing amount. Keyhole welding is often described as the preferable mode for joining advanced materials, but it may not necessarily be applicable to SMAs owing to their specific transformational properties [23]. The close-up micrograph at the fusion boundary (Fig. 3b) reveals a columnar grain structure whose growth was supported by the heat affected zone grains. Occurrence of a partially melted region with an extension of ≈ 50 μm is also evidenced.

Within the fusion zone, a typical dendritic solidification microstructure is obtained, as depicted in Fig. 3c. EDS point analysis (refer to Fig. 3c

Table 1
Transformation temperature of the as-extruded and aged base NiTi-20Zr base material.

Material condition	A_s [°C]	A_f [°C]	M_s [°C]	M_f [°C]
As-extruded	−14	35	n. a.	n. a.
Aged	102	153	97	18

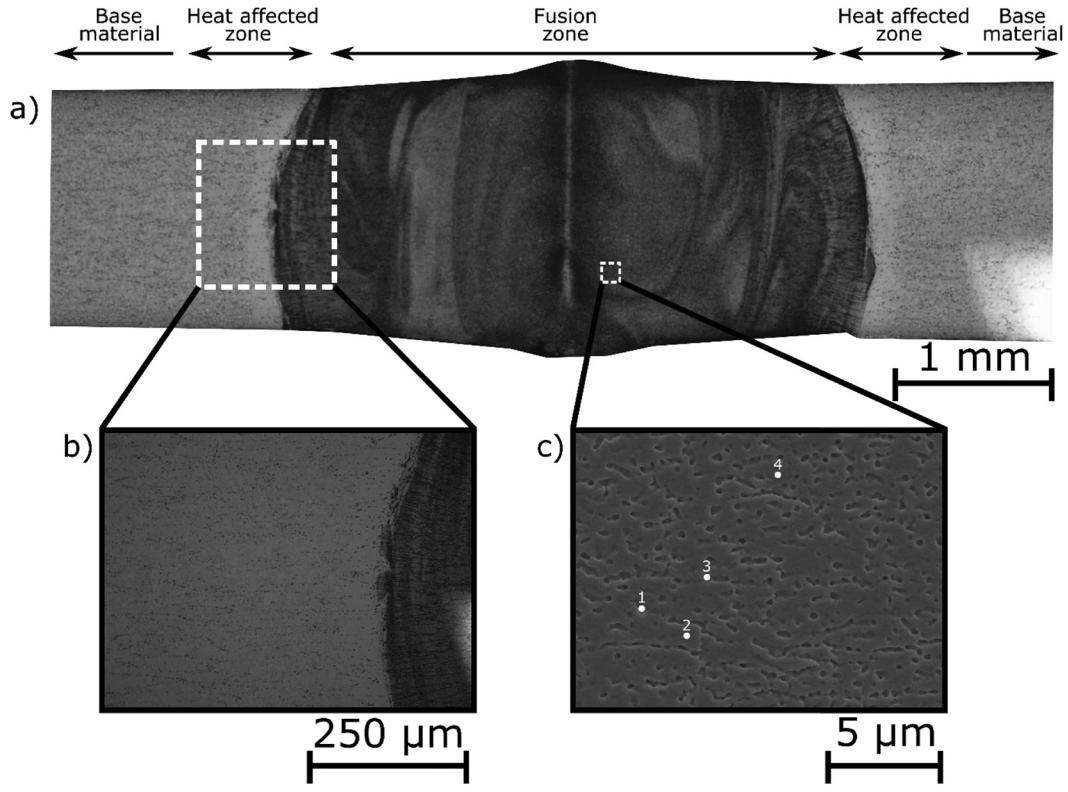

Fig. 3. Optical micrographs of the aged and laser welded NiTi-20Zr alloy: a) overview of the weld cross-section; b) close-up view of the heat affected zone and fusion zone interface; c) scanning electron microscopy image of the fusion zone. The numbers 1 to 4 in c) indicate the locations where energy-dispersive spectroscopy was performed. The results from these measurements are detailed in Table 2.

and Table 2) reveals that the darker roundish regions in points 1 and 3 are Ti-rich (≈ 55 at.% Ti), whereas the surrounding matrix in points 2 and 4 is Ni-rich (≈ 51 at.% Ni). The amount of Zr in the dendritic and interdendritic regions is similar (ranging between 17 and 22 at. %), suggesting that for this element, solute redistribution upon solidification is not significant. Although this elemental segregation may not be detrimental to the joint structural performance, it can have an effect on local functional properties such as transformation temperatures [24]. This is especially relevant to the NiTi-20Zr alloy because minor compositional changes can drastically modify the transformation temperatures and, consequently, their local functional behavior [11]. Hence, the use of post-weld heat treatments to promote chemical homogenization may be beneficial. Although the compositional data shown in Table 2 differ from the target composition, EDS-derived chemistry measurements can come with large errors; hence, this data is used relative to the base material for better comparison with the weld regions.

For a more in-depth analysis of the fusion zone microstructure, a site-specific thin foil was obtained and prepared by FIB. A high-angle annular dark-field imaging (HAADF) image obtained via STEM of the fusion zone is depicted in Fig. 4. In addition to the typical martensite twins [25], sparsely dispersed nanoscale precipitates are visible. EDS mapping and line scan analysis were performed to further clarify the chemical composition of these precipitates (Fig. 4c to f). Based on these measurements, it can be inferred that these features are not the equilibrium precipitates typical of NiTiZr SMAs, such as the H-phase expected in the aged alloys [26]. Rather, two types of precipitates with clearly distinct chemical composition are observed: one, a Zr-rich (≈ 60 at. %) and almost Ni-depleted (≈3 at. %) precipitate (Fig. 4d), and the other, a particle with near-equiatomic composition (Fig. 4e). Although the oxygen content measured during STEM/EDS was low, it is possible that these precipitates are stabilized due to oxygen pickup during welding owing to the very high reactivity of the elements that compose these alloys, especially at high temperatures. At the nanoscale, the martensitic matrix presents a uniform composition for each element (Fig. 4f), with a composition similar to that of the original base material.

A superimposition of the synchrotron diffraction patterns obtained across the joint is shown in Fig. 5. Single diffraction patterns of each region (base material, heat affected and fusion zones) are detailed in Fig. 6. Phase identification of these regions revealed that the base material and heat affected zone are composed of B2 cubic austenite, B19' monoclinic martensite, and orthorhombic H-phase. This is in line with the material's DSC curves, shown in Fig. 2, where the martensite finish is very close to room temperature, explaining the presence of the austenite phase. Additionally, the shift in transformation temperatures after aging is attributed to the H-phase formation, hence the H-phase peaks are present in the spectra of Fig. 5.

In the fusion zone, only the monoclinic martensite and the cubic austenite are observed. The H-phase dissolves around 780 °C [27], which is easily exceeded during welding, and upon solidification it does not form due to the rapid cooling rates typical of the laser welding process. Moreover, given the absence of H-phase in this region, the transition temperature shifts to lower values, hence the austenite peaks are more

Table 2
Energy-dispersive spectroscopy (EDS) point analysis from the fusion zone. The locations for the EDS measurements are detailed in Fig. 3c. The base material composition as determined by scanning electron microscopy (SEM)/EDS is also reported.

EDS location	Ni [at.%]	Ti [at.%]	Zr [at.%]
1 – dendritic space	22.8	54.8	22.4
2 – interdendritic space	51.6	30.5	17.9
3 – dendritic space	22.0	55.3	22.7
4 – interdendritic space	51.3	31.1	17.6
Base material	51.9	29.0	19.1

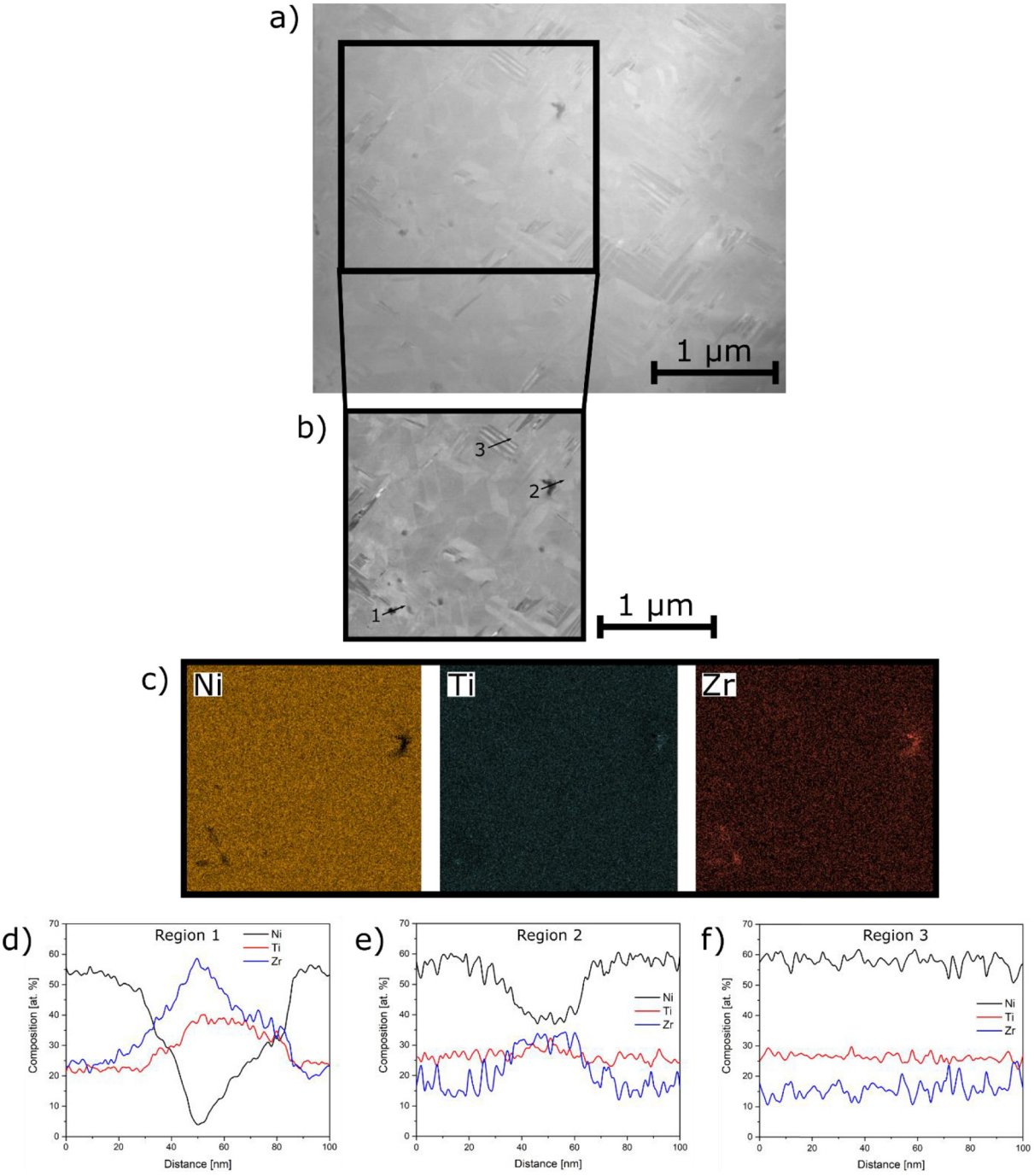

Fig. 4. a) High-angle annular dark-field imaging (HAADF) image of the fusion zone of the NiTi-20Zr joint; b) detail of a) where energy-dispersive spectroscopy mapping and line scans were performed; c) elemental mapping of Ni, Ti, and Zr in the insert of a); d) to f) energy-dispersive line scans of regions of interest detailed in b).

pronounced in this condition. For reference, the refined lattice parameters of austenite, martensite, and H-phase that compose the starting aged alloy are detailed in Table 3.

From the diffraction patterns depicted in Figs. 5 and 6, the microstructural differences between the aged base material, heat affected zone, and fusion zone are evident. The base material is composed of austenite, martensite, and H-phase, as expected for the heat treatment conditions imposed upon the material prior to welding [28]. In the heat affected zone, the phase propensity between the martensite and austenite varies, as evidenced by changing peak intensities. Within this region, the weld thermal cycle experienced by the material resembles a fast, non-equilibrium heat treatment capable of modifying the microstructure of the material. Previous works on the effect of heat treatments on the microstructure evolution of NiTi alloys have shown similar behavior [29,30]. As a result, peak intensities change, and H-phase peaks that previously overlapped with broad martensite peaks reappear. In the fusion zone, solely diffraction peaks corresponding to austenite and martensite are indexed. This was expected, as melting of the alloy within this region completely dissolves the H-phase precipitates and the fast cooling conditions upon solidification do not allow for their re-precipitation. The representative diffraction patterns of each region of the material, shown in Fig. 6, demonstrate that the material texture is modified as a result of the welding process.

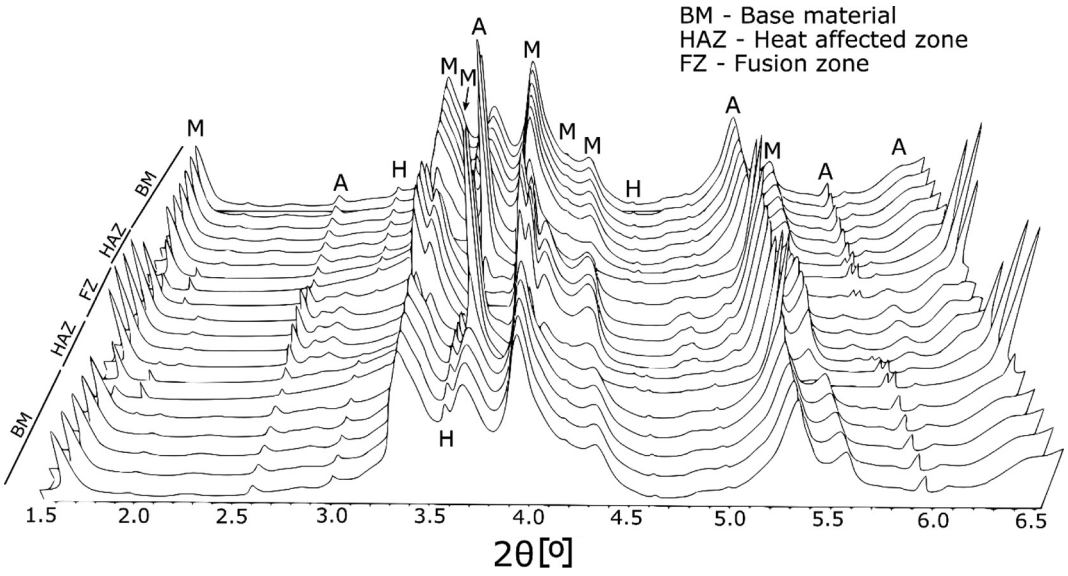

Fig. 5. Series of synchrotron X-ray diffraction patterns throughout the welded NiTi-20Zr alloy. The major austenite (A), martensite (M), and H-phase (H) diffraction peaks are labelled.

To evaluate how the weld thermal cycle impacted the volume fractions of austenite, martensite, and H-phase across the joint, Rietveld refinement was performed. Typical Rietveld refinement plots for the base material, heat affected and fusion zones are depicted in Fig. 7. It should be noticed that the bottom part of Fig. 7 a), b) and c) correspond to the conventional bidimensional Debbye-Scherrer diffraction rings converted from from polar to cartesian coordinates. The top side in each section of Fig. 7 corresponds to the simulated diffraction pattern after Rietveld refinement. The major austenite and martensite diffraction peaks are also marked.

The evolution of the volume fractions of all three phases across the welded joint is shown in Fig. 8. The base material consists primarily of the martensite phase with a volume fraction of ~85%. This is not surprising given that the martensite finish temperature of the aged NiTi-20Zr alloy is near room temperature (18 °C), as shown by the DSC curves (refer to Fig. 2), while the synchrotron measurements were performed at around ≈25 °C. One should note the asymmetry in both the cooling and heating transformation peaks that push the transformation temperatures on the aged base material to near room temperature (upon cooling), thus justifying the presence of roughly ≈ 8% of austenite at room temperature as determined by Rietveld refinement of the diffraction data obtained from the base material.

Of more significance is the amount of H-phase present, which is rarely measured and reported in the literature. The base material contained an H-phase volume fraction of ≈ 7%, after the 550 °C/3 h heat treatment performed prior to welding. This precipitation phenomenon locally modifies the matrix chemical composition, promoting a significant rise in transformation temperatures, thus allowing for more martensite to remain stable at room temperature.

When probing the heat affected zone, the H-phase volume fraction starts to decrease consistently toward the heat affected zone/fusion zone interface. Concomitant with the decrease of H-phase, there is an increase in the austenite volume fraction with a corresponding decrease in martensite. As some of the H-phase dissolves, the transformation temperatures decrease, resulting in more austenite at the test (room) temperature. It is noted that a recent study by Benafan et al. [27] has shown that the H-phase is stable up to approximately 780 °C in a NiTi-20Hf alloy. In the current study, it is suggested that the H-phase dissolves at higher temperatures attained in this region (e.g., > 1000 °C). This inconsistency may be attributed to the addition of Zr as opposed to Hf, where the precipitation kinetics have been shown to be very different [10]. Additionally, the heating rates used in Benafan et al. were in the order of 10 °C/min, whereas the heating rates attained during laser welding are orders of magnitude higher [31], even outside the fusion zone. As such, the non-equilibrium conditions found during laser welding can promote the stability of H-phase at temperatures above those obtained for near-equilibrium heating conditions. The H-phase did not fully dissolve in the heat affected zone, although higher dissolution of this phase occurred when approaching the fusion boundaries, where a minimum of ≈ 1.5% of H-phase was measured. No H-phase was detected in the fusion zone.

The effect of welding on the microhardness across the joint was measured using bidimensional hardness mapping, as shown in Fig. 9. The higher hardness is found in the base material (≈ 500 HV), which results from the strengthening effect induced by H-phase precipitation after aging at 550 °C for 3 h. In the heat affected zone, a decay to ≈ 430 HV occurs. This is attributed to the partial dissolution of the H-phase, as identified from the synchrotron X-ray diffraction experiments. Still within the heat affected zone, a more dramatic decrease is found when approaching the fusion boundary, where the hardness drops to ≈ 390 HV. Here, this decrease can be attributed to two concomitant effects: i) partial H-phase dissolution, which is more pronounced closer to the fusion zone, and ii) increase of the material grain size, which occurs during fusion-based welding as a result of the high peak temperatures experienced by the material. In the fusion zone, the hardness increases back up to ≈ 420 HV. This increase is attributed to the presence of higher volume fraction of the austenite phase (as opposed to dominantly martensite phase in the heat affected zone) as a result of the shift in transformation temperatures, when the H-phase completely dissolves.

Overall, it is evidenced that the microstructure changes resulting from laser welding have a marked effect on the microhardness across the fusion zone.

3.2. Mechanical testing

Mechanical testing was performed on the aged and welded NiTi-20Zr samples as follows: at room temperature with both austenite and martensite, and at 200 °C with austenite only. Both cases contained the non-transforming H-phase. As detailed in the experimental procedure, a load/unload cycle between 500 and 800 MPa was applied at both temperatures, as shown in Fig. 10. For the room temperature tests (Fig. 10a and b), a reference unwelded sample (S1) was deformed to 700 MPa followed by unloading to 0 MPa in order to capture both the

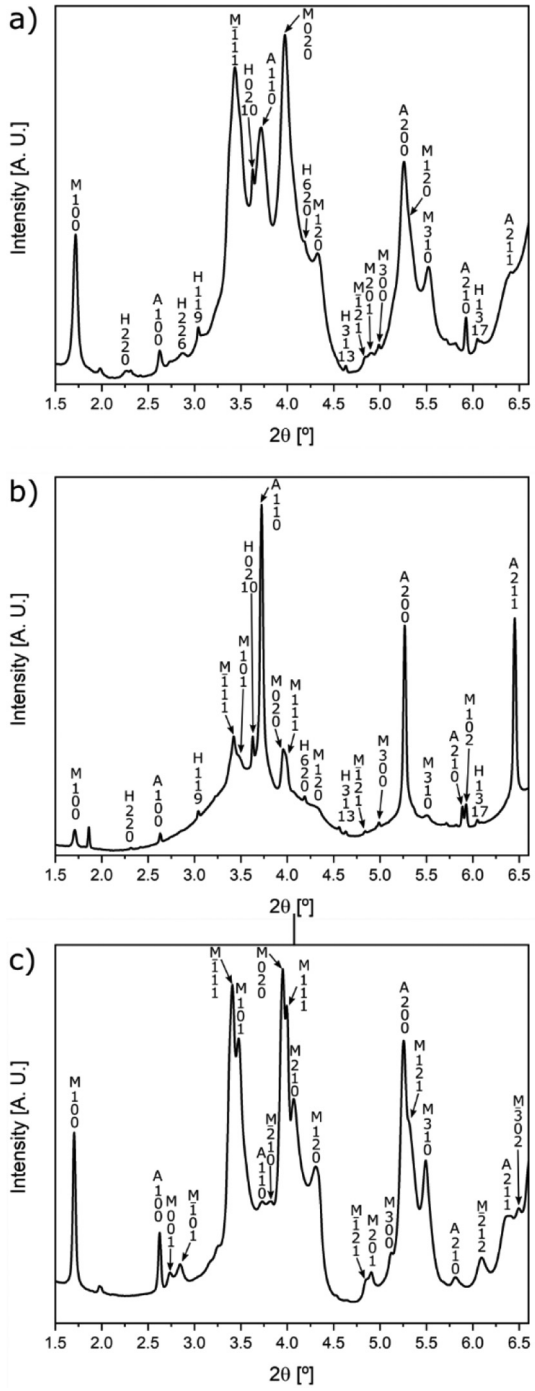

Fig. 6. Individual synchrotron X-ray diffraction patters of the aged NiTi-20Zr alloy in the: a) base material; b) heat affected zone; c) fusion zone. A, M, and H represent the austenite, martensite, and H-phase peaks, respectively, for the associated (*hkl*) planes.

elastic response and the reorientation/detwinning process in the martensite phase. The welded sample S2 (not shown here) was also set to reach 700 MPa but failed prematurely at 647 MPa at the weld section.

Table 3
Refined lattice parameters of martensite, austenite, and H-phase in the aged (550 °C/3 h) base material.

Phase	a [nm]	b [nm]	c [nm]	α [°]	β [°]	γ [°]
Austenite	3.0756	a = b = c	a = b = c	90	90	90
Martensite	4.9255	4.0856	3.2788	90	105.2780	90
H-phase	12.3826	9.0164	25.8370	90	90	90

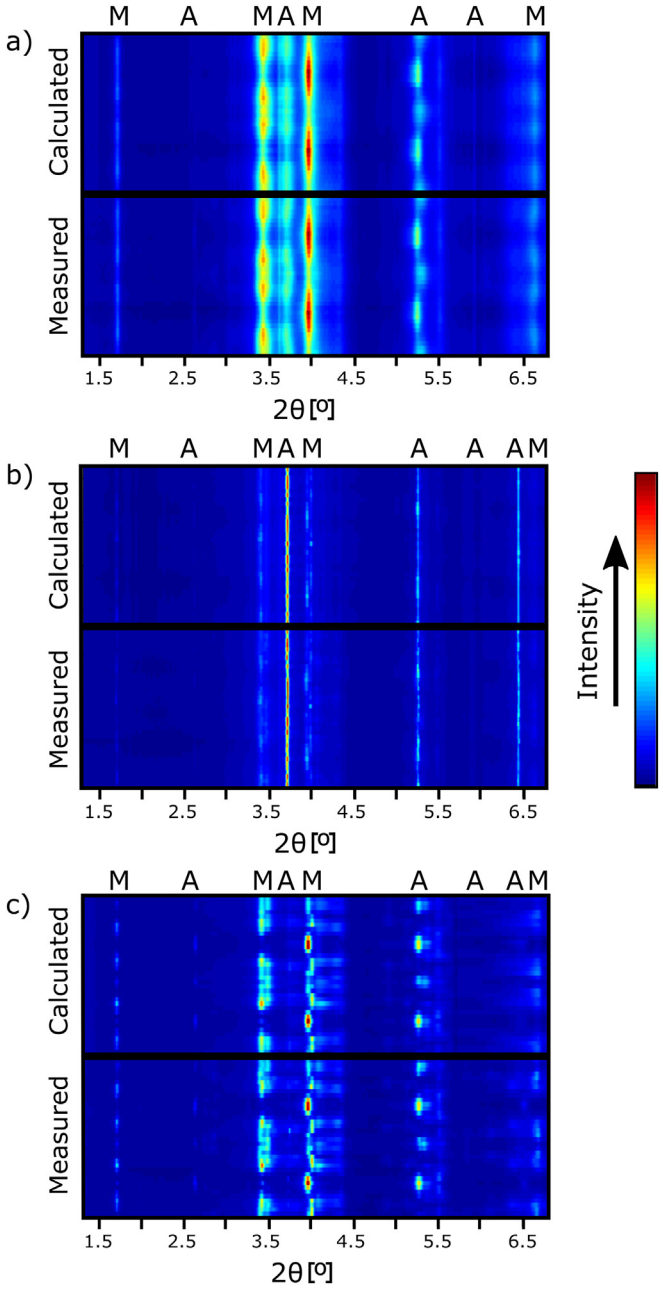

Fig. 7. Representative 2D Rietveld refinement plots of aged NiTi-20Zr alloy in: a) base material; b) heat affected zone; c) fusion zone. The most intensive austenite (A) and martensite (M) diffraction peaks are marked.

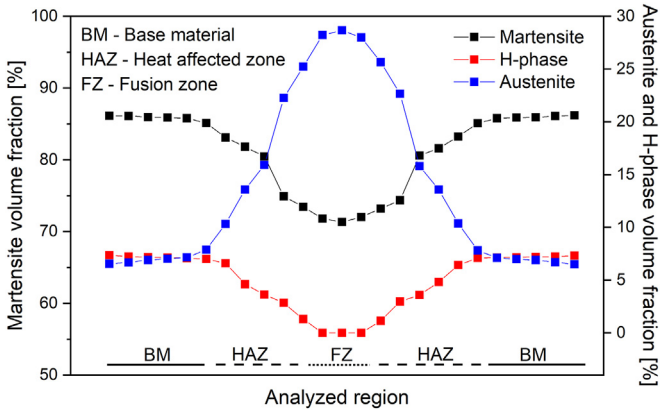

Fig. 8. Evolution of austenite, martensite, and H-phase volume fractions across the aged and welded NiTi-20Zr joints.

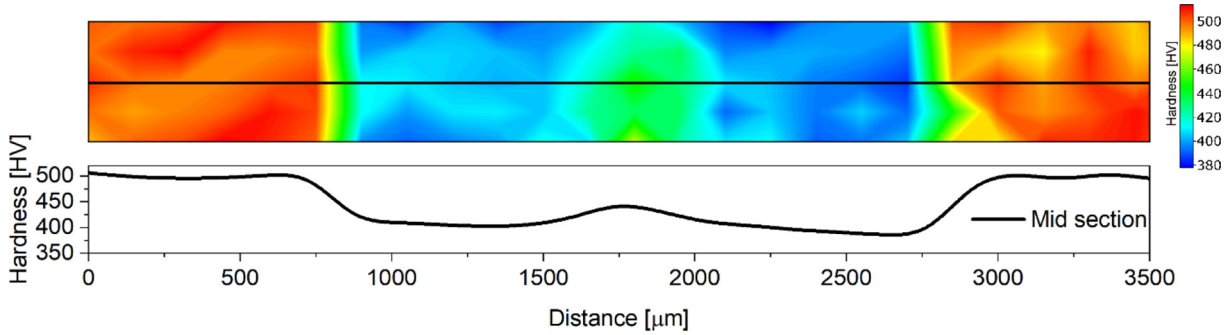

Fig. 9. Hardness mapping across the welded joint with a representative line scan obtained at a middle height of the sample (black line hardness map).

A second welded sample (S3) was also deformed, but this time only to 500 MPa in order to capture the unloading behaviors. The overall responses were very similar, showing an initial elastic (linear) region followed by a non-linear elastic region mostly attributed to martensite reorientation and detwinning, as is commonly observed in this family of alloys. The early onset of fracture in sample S2 is largely attributed to (i) residual stresses that are common in the weld region, (ii) the dendritic structure, and (iii) potentially brittle non-metallic inclusions that may have formed in the fusion zone, as shown in Fig. 4. Nonetheless, the stresses imparted on the welded samples are significantly above those typically used in actuator applications.

The high temperature tests performed at 200 °C were targeted to probe the austenite phase and the formation of stress-induced martensite, evidenced by the superelastic curve (refer to Fig. 10 c and d). The reference unwelded sample (S4) was deformed to 800 MPa and unloaded, which showed the classical superelastic response with 100% recovery. Given that sample S2 failed prematurely, the high temperature test of the welded joint (reference S5) was limited to 500 MPa, and it is shown to follow the reference material seamlessly. Upon unloading, no residual strains were observed, but this is somewhat expected given that the stress levels used on the welded sample were not high enough to induce large strains. Higher imposed stresses (and consequently strains) can be expected to lead to some irrecoverable strain, even when testing within the elastic and stress-induced martensite regions, due to the graded microstructure resulting from the laser welding process. While outside the scope of the present

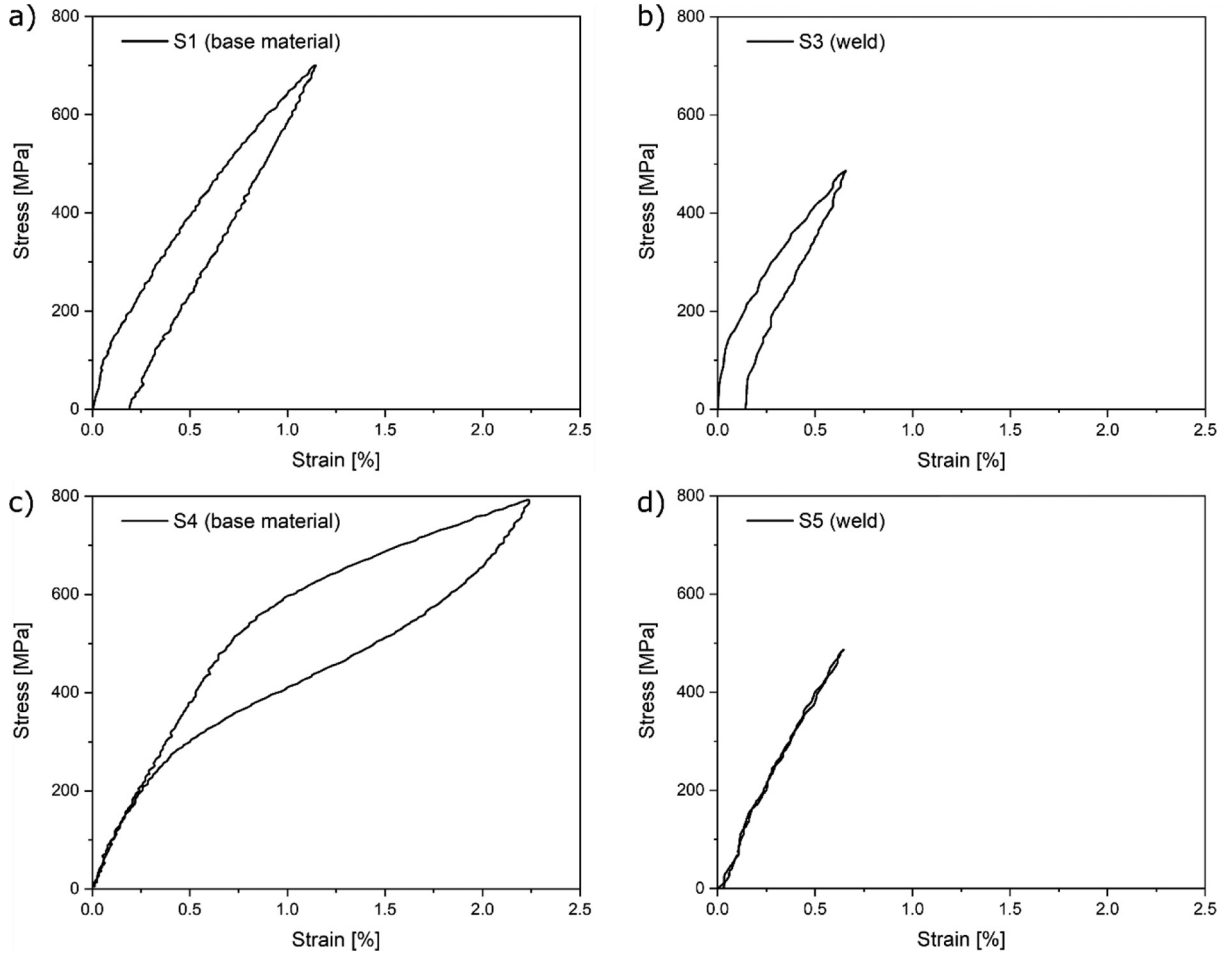

Fig. 10. Stress-strain responses of aged NiTi-20Zr alloy. a) and b): Room temperature tests corresponding to reference base material sample (S1) and welded joint (S3) loaded to 500 MPa and unloaded; c) and d): high-temperature temperature (200 °C) tests corresponding to reference base material sample (S4) and welded joint (S5).

work, this expectation is based on existing knowledge of welding of NiTi-based SMAs [29].

4. Conclusions

In this work, the first report on welding of a Ni-rich NiTi-20Zr high temperature shape memory alloy is presented. The microstructure evolution due to the laser welding thermal cycle across the joint was evaluated combining optical and electron microscopies, synchrotron X-ray diffraction, microhardness mapping and mechanical testing in the low (room temperature) and high temperature regimes. The following conclusions can be made:

- Laser welding promoted partial dissolution of the pre-existent H-phase precipitates in the heat affected zone, leading to a hardness decrease to ~390 HV, as compared to the precipitation-strengthened base material's hardness of ~500 HV.
- The fusion zone consisted of a dendritic microstructure with no H-phase precipitates. X-ray diffraction showed that this region is mostly austenitic due to the dissolution of the H-phase and concomitant shift of transformation temperature to lower temperatures. The hardness also decreased in this region due to the lack of a precipitation-strengthening mechanism.
- Although not affected by the welding process, the H-phase volume fraction in the base metal was found to be near 7% after aging at 500 °C for 3 h, shedding some light on the role of aging and precipitation strengthening.
- Mechanical loading of the aged and welded NiTi-20Zr up to 500 MPa was performed at room temperature and at 200 °C with no fracture, and exhibited behavior identical to that of the reference base material. Loading to higher stresses resulted in fracture around 647 MPa, largely attributed to the dendritic structures in the fusion zone and residual stresses typically remnant from the welding process.
- The aged NiTi-20Zr alloy exhibited good laser weldability, which can open new doors for the use of these materials in actuation-based applications.

The raw/processed data required to reproduce these findings cannot be shared at this time as the data also forms part of an ongoing study.

CRediT authorship contribution statement

J.P. Oliveira: Conceptualization, Data curation, Formal analysis, Investigation, Methodology, Project administration, Resources, Supervision, Validation, Visualization, Writing - original draft. **Jiajia Shen**: Data curation, Investigation. **J.D. Escobar**: Investigation, Writing - review & editing. **C.A.F. Salvador**: Investigation, Writing - review & editing. **N. Schell**: Investigation, Writing - review & editing. **N. Zhou**: Investigation, Writing - review & editing. **O. Benafan**: Data curation, Formal analysis, Resources, Validation, Investigation, Writing - review & editing.

Declaration of Competing Interest

The authors declare that they have no known competing financial interests or personal relationships that could have appeared to influence the work reported in this paper.

The authors declare the following financial interests/personal relationships which may be considered as potential competing interests:

Acknowledgments

JPO and JS acknowledge Fundação para a Ciência e a Tecnologia (FCT - MCTES) for its financial support via the project UIDB/00667/2020 (UNIDEMI). The research leading to this result has been supported by the project CALIPSOplus under the Grant Agreement 730872 from the EU Framework Programme for Research and Innovation HORIZON 2020 (proposal I-20160912). OB acknowledges support from the NASA Aeronautics Research Mission Directorate (ARMD) Transformational Tools and Technologies (TTT) project. OB thanks Leo Wood (student intern) for assistance with mechanical testing.

References

[1] K. Otsuka, X. Ren, Physical metallurgy of Ti-Ni-based shape memory alloys, Prog. Mater. Sci. 50 (2005) 511–678, https://doi.org/10.1016/j.pmatsci.2004.10.001.
[2] L. Petrini, F. Migliavacca, Biomedical applications of shape memory alloys, J. Metall. 2011 (2011) 1–15, https://doi.org/10.1155/2011/501483.
[3] J. Van Humbeeck, S. Kustov, Active and passive damping of noise and vibrations through shape memory alloys: applications and mechanisms, Smart Mater. Struct. 14 (2005) S171–S185, https://doi.org/10.1088/0964-1726/14/5/001.
[4] J. Van Humbeeck, Non-medical applications of shape memory alloys, Mater. Sci. Eng. A 273–275 (1999) 134–148, https://doi.org/10.1016/S0921-5093(99)00293-2.
[5] Z. Wang, J. Chen, C. Besnard, A.M. Korsunsky, Microstructure evolution in a severely cold-worked NiTi wire during ageing treatment: an in situ neutron diffraction study, Mater. Lett. 281 (2020) 128676, https://doi.org/10.1016/j.matlet.2020.128676.
[6] B.C. Hornbuckle, T.T. Sasaki, G.S. Bigelow, R.D. Noebe, M.L. Weaver, G.B. Thompson, Structure-property relationships in a precipitation strengthened Ni-29.7Ti-20Hf (at%) shape memory alloy, Mater. Sci. Eng. A 637 (2015) 63–69, https://doi.org/10.1016/j.msea.2015.03.123.
[7] D.R. Coughlin, L. Casalena, F. Yang, R.D. Noebe, M.J. Mills, Microstructure–property relationships in a high-strength 51Ni–29Ti–20Hf shape memory alloy, J. Mater. Sci. 51 (2016) 766–778, https://doi.org/10.1007/s10853-015-9400-7.
[8] A. Shuitcev, R.N. Vasin, M. Balagurov, L. Li, I.A. Bobrikov, Y.X. Tong, Thermal expansion of martensite in Ti29.7Ni50.3Hf20 shape memory alloy, Intermetallics 125 (2020) 18–20, https://doi.org/10.1016/j.intermet.2020.106889.
[9] A. Evirgen, I. Karaman, R.D. Noebe, R. Santamarta, J. Pons, Effect of precipitation on the microstructure and the shape memory response of the Ni50.3Ti29.7Zr20 high temperature shape memory alloy, Scr. Mater. 69 (2013) 354–357, https://doi.org/10.1016/j.scriptamat.2013.05.006.
[10] M. Carl, B. Van Doren, M.L. Young, In situ synchrotron radiation X-ray diffraction study on phase and oxide growth during a high temperature cycle of a NiTi-20 at. % Zr high temperature shape memory alloy, Shape Mem. Superelast. 4 (2018) 174–185, https://doi.org/10.1007/s40830-018-0149-0.
[11] G.S. Bigelow, O. Benafan, A. Garg, R. Lundberg, R.D. Noebe, Effect of composition and applied stress on the transformation behavior in NiXTi80−XZr20 shape memory alloys, Shape Mem. Superelast. 5 (2019) 444–456, https://doi.org/10.1007/s40830-019-00259-w.
[12] G.S. Bigelow, O. Benafan, A. Garg, R.D. Noebe, Effect of Hf/Zr ratio on shape memory properties of high temperature Ni50.3Ti29.7(Hf,Zr)20 alloys, Scr. Mater. 194 (2021), 113623, https://doi.org/10.1016/j.scriptamat.2020.11.008.
[13] J.P. Oliveira, N. Schell, N. Zhou, L. Wood, O. Benafan, Laser welding of precipitation strengthened Ni-rich NiTiHf high temperature shape memory alloys: microstructure and mechanical properties, Mater. Des. 162 (2019) 229–234, https://doi.org/10.1016/j.matdes.2018.11.053.
[14] Z. Altounian, J.O. Strom-Olsen, D.H. Ryan, Structure origin of a transition of classic-to-avalanche nucleation in Zr-Cu-Al bulk metallic glasses, Scr. Mater. 163 (2019) 166–167, https://doi.org/10.1016/j.scriptamat.2019.01.005.
[15] J.P. Oliveira, Z. Zeng, S. Berveiller, D. Bouscaud, F.M. Braz Fernandes, R.M. Miranda, N. Zhou, Laser welding of cu-Al-be shape memory alloys: microstructure and mechanical properties, Mater. Des. 148 (2018) 145–152, https://doi.org/10.1016/j.matdes.2018.03.066.
[16] J.P. Oliveira, Z. Zeng, C. Andrei, F.M. Braz Fernandes, R.M. Miranda, A.J. Ramirez, T. Omori, N. Zhou, Dissimilar laser welding of superelastic NiTi and CuAlMn shape memory alloys, Mater. Des. 128 (2017) 166–175, https://doi.org/10.1016/j.matdes.2017.05.011.
[17] A.P. Hammersley, S.O. Svensson, M. Hanfland, A.N. Fitch, D. Hausermann, Two-dimensional detector software: from real detector to idealised image or two-theta scan, High Pressure Res. 14 (1996) 235–248, https://doi.org/10.1080/08957959608201408.
[18] A.P. Hammersley, S.O. Svensson, A. Thompson, Calibration and correction of spatial distortions in 2D detector systems, Nucl. Inst. Methods Phys. Res. Sect. A Accel. Spect. Detect. Assoc. Equip. 346 (1994) 312–321, https://doi.org/10.1016/0168-9002(94)90720-X.
[19] L. Lutterotti, S. Matthies, H.-R. Wenk, A.S. Schultz, J.W. Richardson, Combined texture and structure analysis of deformed limestone from time-of-flight neutron diffraction spectra, J. Appl. Phys. 81 (1997) 594, https://doi.org/10.1063/1.364220.
[20] H.-R. Wenk, L. Lutterotti, P. Kaercher, W. Kanitpanyacharoen, L. Miyagi, R. Vasin, Rietveld texture analysis from synchrotron diffraction images. II. Complex multiphase materials and diamond anvil cell experiments, Powder Diffract. 29 (2014) 1–13, https://doi.org/10.1017/S0885715614000360.
[21] L. Lutterotti, R. Vasin, H.-R. Wenk, Rietveld texture analysis from synchrotron diffraction images. I. Calibration and basic analysis, Powder Diffract. 29 (2014) 76–84, https://doi.org/10.1017/S0885715613001346.
[22] C.X. Zhao, C. Kwakernaak, Y. Pan, I.M. Richardson, Z. Saldi, S. Kenjeres, C.R. Kleijn, The effect of oxygen on transitional Marangoni flow in laser spot welding, Acta Mater. 58 (2010) 6345–6357, https://doi.org/10.1016/j.actamat.2010.07.056.
[23] J.P. Oliveira, D. Barbosa, F.M.B. Fernandes, R.M. Miranda, Tungsten inert gas (TIG) welding of Ni-rich NiTi plates: functional behavior, Smart Mater. Struct. 25 (2016), 03LT01, https://doi.org/10.1088/0964-1726/25/3/03LT01.

[24] J.P. Oliveira, A.J. Cavaleiro, N. Schell, A. Stark, R.M. Miranda, J.L. Ocana, F.M. Braz Fernandes, Effects of laser processing on the transformation characteristics of NiTi: a contribute to additive manufacturing, Scr. Mater. 152 (2018) 122–126, https://doi.org/10.1016/j.scriptamat.2018.04.024.
[25] A. Evirgen, I. Karaman, R. Santamarta, J. Pons, C. Hayrettin, R.D. Noebe, Relationship between crystallographic compatibility and thermal hysteresis in Ni-rich NiTiHf and NiTiZr high temperature shape memory alloys, Acta Mater. 121 (2016) 374–383, https://doi.org/10.1016/j.actamat.2016.08.065.
[26] R. Santamarta, R. Arróyave, J. Pons, A. Evirgen, I. Karaman, H.E. Karaca, R.D. Noebe, TEM study of structural and microstructural characteristics of a precipitate phase in Ni-rich Ni-Ti-Hf and Ni-Ti-Zr shape memory alloys, Acta Mater. 61 (2013) 6191–6206, https://doi.org/10.1016/j.actamat.2013.06.057.
[27] O. Benafan, G.S. Bigelow, A. Garg, R.D. Noebe, D.J. Gaydosh, R.B. Rogers, Processing and scalability of NiTiHf high temperature shape memory alloys, Shape Mem. Superelast. (2020) (in press).
[28] A. Evirgen, I. Karaman, J. Pons, R. Santamarta, R.D. Noebe, Role of nano-precipitation on the microstructure and shape memory characteristics of a new Ni50.3Ti34.7Zr15 shape memory alloy, Mater. Sci. Eng. A 655 (2016) 193–203, https://doi.org/10.1016/j.msea.2015.12.076.
[29] J.J. Marattukalam, V.K. Balla, M. Das, S. Bontha, S.K. Kalpathy, Effect of heat treatment on microstructure, corrosion, and shape memory characteristics of laser deposited NiTi alloy, J. Alloys Compd. 744 (2018) 337–346, https://doi.org/10.1016/j.jallcom.2018.01.174.
[30] S. Takabayashi, K. Tanino, K. Kitagawa, Heat treatment effect on transformation properties of TiNi shape memory alloy film, J. Soc. Mater. Sci. Jpn. 46 (1997) 220–224, https://doi.org/10.2472/jsms.46.12Appendix_220.
[31] J.P. Oliveira, T.G. Santos, R.M. Miranda, Revisiting fundamental welding concepts to improve additive manufacturing: from theory to practice, Prog. Mater. Sci. 107 (2019) 100590, https://doi.org/10.1016/j.pmatsci.2019.100590.